On the acoustic optimality of leading-edge serration profiles

Benshuai Lyu[a,*], Lorna J. Ayton[a], Paruchuri Chaitanya[b]

[a] *Department of Applied Mathematics and Theoretical Physics, University of Cambridge, Cambridge CB3 0WA, UK*
[b] *University of Southampton, Southampton SO17 1BJ, UK*

Abstract

Leading-edge serrations are studied extensively as a way of reducing leading-edge noise and have been shown to be able to reduce leading-edge noise significantly. Previous experiments showed that different serration geometries have different noise reduction capabilities. However, the optimal serration geometry has not been known. Consequently, there are no guides that can be used at the design stage of serrations. In this paper, by performing an asymptotic analysis, we show that in order to achieve greater noise reduction in the high frequency regime ($k_1 h \gg 1$, where k_1 denotes the streamwise hydrodynamic wavenumber and h half of the root-to-tip amplitude of serrations), the serration profile cannot have stationary points. Therefore, piecewise smooth profiles free of stationary points are more desirable. Moreover, we show that greater noise can be achieved in the high frequency regime by using serrations that are sharper around the non-smooth points. The underlying physical mechanisms of these findings are discussed. Based on these findings, a new type of serration profile is proposed, and analytical model evaluations confirm its improved acoustic performance in the frequency range of interest. At low frequencies, a slight deterioration may be expected, but this is often negligible. To verify the conclusion drawn from the analysis, we perform an experimental study to investigate the acoustic performance of this new serration design. The results show that it is indeed superior than conventional sawtooth serrations. For example, a remarkable 7 dB additional noise reduction is observed in the intermediate frequency range with no perceivable noise increase elsewhere. The trends predicted by the analysis are well validated by the experiment. It is expected that these findings can serve as an essential guide for designing serrations, and lead to more acoustically

*Corresponding author
Email address: bl362@cam.ac.uk (Benshuai Lyu)

optimized serration geometries.

Keywords: aeroacoustics; noise control; scattering

1. Introduction

Aerofoil noise is of great importance in a wide range of applications, such as wind turbines, aero-engines, high-speed propellers and fans. The overall aerofoil noise is complicated, consisting of more than one physical mechanisms of noise generation [5, 32]. These include the noise due to the scattering of the turbulent boundary layer by the trailing edge, the tip vortex formation noise, and the noise due to the scattering of incoming turbulence/unsteady gusts by the leading edge etc.

In many applications, in particular where more than one row of rotors are installed, the scattering of the unsteady flow by an aerofoil leading edge plays a crucial role in the noise generation. For example, in contra-rotating open rotor systems, the wakes from the front row impinge on the downstream blades. This leads to a strong interaction between the unsteady wakes and the leading edge of the downstream blades, resulting in efficient noise radiation. This noise is often referred to as leading-edge noise, and it is considered as the main source in similar multi-row rotor systems such as the jet engines. The problem of leading-edge noise is especially important in modern aeroengines with ultra-high bypass ratios, where the distance between the rotor and stator becomes increasingly short.

The research on leading-edge noise dates back to the 1940s. As one of the early attempts, Sears [36] investigated the aerodynamic response of a flat plate subject to an sinusoidal gust. This study focused on an incompressible flow, and this was extended to compressible flows by Graham [14] and Amiet [1]. In Amiet's work, the acoustic response due to a single sinusoidal incoming gusts was obtained using the Schwarzschild method and the theory of Kirchhoff and Curle [12]. The far-field sound was then related to the wavenumber spectral density of the vertical velocity fluctuations. Provided that this wavenumber spectral density can be modelled accurately, the far-field sound can be predicted robustly using Amiet's approach and agrees well with experimental results. Amiet's approach has been shown to work fairly well and become an important method for following studies.

Due to the importance of leading-edge noise in many applications, techniques for its reduction have been of research interest for many years. One of the most widely studied approaches is to use bio-inspired serrated leading edges [6, 13, 28].

One of the earliest studies of the acoustic effects of leading edge serrations is that by Soderman [38] in the 1970s, and some recent studies such as Clair et al. [10] and Roger et al. [33]. It has been shown experimentally that the use of serrations leads to reduced leading-edge noise and improved aerodynamic performance at high angles of attack [16, 27]. The acoustic benefit of using serrations was also studied numerically in a number of recent works, such as those by Lau et al. [18], Kim et al. [17] and Turner and Kim [39]. Lau et al. [18]'s work showed that the dimensionless quantity $\tilde{k}_1\tilde{h}$, where $\tilde{k}_1$ denotes the hydrodynamic wavenumber in the streamwise direction and $\tilde{h}$ denotes half of the root-to-tip length of serrations, plays an important role in determining the effectiveness of the serrations. Kim et al. [17] argued that both source cut-off and destructive interference effects contributed to the noise reduction achieved by using serrations. The recent work of Lyu and Azarpeyvand [19] extended Amiet's work and developed a noise prediction model for serrated leading edges. It showed that the destructive interference plays a central role in the noise reduction, and proposed two geometric criteria for designing effective serrations.

Though the serrations have been shown to be able to reduce leading-edge noise effectively, both experimentally and numerically with a number of designs proposed (see for example Chaitanya et al. [8, 9], Chaitanya and Joseph [7]), it remains unclear what serration geometry leads to the maximum noise reduction. Previous experiment mostly focused on serrations of sinusoidal profiles [16, 27]. However, a recent study [8, 9] showed that a new type of serration geometry, which was formed by a superposition of two sinusoidal profiles of different frequency, amplitude and phase, could result in greater noise reduction than the single wavelength serrations for specific frequency bands. Note that this acoustic performance improvement occurred in a relative low frequency band and there was little change to the noise levels at high frequencies. Nevertheless, this study showed that it is possible to achieve greater noise reduction via changing the serration geometries. It is therefore desirable to understand how the serration geometry changes the acoustic performance and how we can design more acoustically effective serrations.

In this paper, we address this need. We do so by using the recent model developed by Ayton and Chaitanya [3, 4] and then examining the asymptotic behaviour of the scattered noise power spectral density. In the following sections, in order to introduce necessary notations, the essential steps to reproduce the results obtained by Ayton and Chaitanya [4] are presented first in section 2. Section 3 derives the formula for the sound power spectral density in the far-field, based on which the following section performs an asymptotic analysis

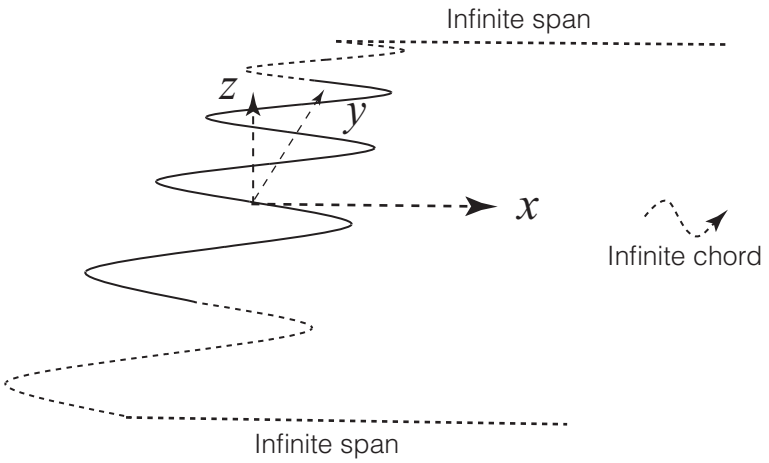

Figure 1: Schematic illustration of the leading-edge serration and the Cartesian coordinates.

to assess the acoustic performances of different serration geometries. The last section concludes this paper and lists some of our future work.

2. Analysis

The serrated aerofoil is assumed to be a semi-infinite plate [1, 31, 19] placed in a uniform incoming flow of density $\tilde{\rho}$ and velocity $\tilde{U}$ at zero angle of attack, as shown in figure 1. When the angle of attack is not zero, or the aerofoil has both finite thickness and camber, the incoming turbulence experiences a distortion process [25, 26, 35]. This is likely to affect the spectrum of the incoming turbulence; however, as far as the acoustic scattering is concerned, the assumptions of zero angle of attack and flat plate are likely to be permissible and we may use the frozen-turbulence assumption in the subsequent development of models. In addition, the speed of sound is assumed to be uniformly $\tilde{c}_0$. In the rest of this paper, the serration wavelength $\tilde{\lambda}$ is used to normalise the length dimension, while $\tilde{\rho}$ and $\tilde{U}$ are used to non-dimensionalize other dynamic variables such as the velocity potential and pressure. For example the angular frequency $\tilde{\omega}$ is non-dimensionalized by $\omega = \tilde{\omega}\tilde{\lambda}/\tilde{U}$. In the rest of this paper, unless noted otherwise, all the quantities without tildes are dimensionless.

We restrict our attention to periodic serrations. Because the geometric parameters are normalised by the serration wavelength, the serrations have a period 1. The normalised root-to-tip length is $2h$. Let x, y, z denote the streamwise, spanwise and normal to the plate directions, respectively. The coordinate origin is fixed in the middle between the root and tip. In such a coordinate frame,

the serration profile can be described by $hF(y)$, where $F(y)$ is a single-valued function that has a maximum value 1 and minimum value -1. Moreover, we require 1 to be the smallest period. Other than these constraints, the function $F(y)$ is arbitrary.

When the turbulence in the mean flow passes the leading edge, a scattered potential flow is induced. The scattered potential ensures appropriate boundary conditions to be satisfied. In the leading-edge noise problem, the vertical velocity fluctuation is of our primary concern. The turbulence in the mean flow consists of a wide range of time and length scales. However, one can always perform a Fourier Transformation on the incoming vertical velocity field, such that one only needs to consider a harmonic gust

$$w_i = w_0 \mathrm{e}^{\mathrm{i}(-\omega t + k_1 x + k_2 y)}, \tag{1}$$

where t denotes time (normalised, so are the following quantities unless noted otherwise), w_0 the velocity fluctuation in the z direction, ω the angular frequency and k_1 and k_2 the wavenumbers in the streamwise and spanwise directions, respectively. The turbulence is assumed to be frozen and convects downstream at the speed $\tilde{U}$. Therefore, one has $k_1 = \omega$.

Let ϕ_s denote this scattered velocity potential. One can show that, with a uniform mean flow, ϕ_s satisfies the convective wave equation [2]

$$\nabla^2 \phi_s - M^2 \left(\frac{\partial}{\partial t} + \frac{\partial}{\partial x} \right)^2 \phi_s = 0, \tag{2}$$

where $M = \tilde{U}/\tilde{c}_0$. To ensure that the normal velocity on the plate vanishes, we require

$$\left. \frac{\partial \phi_s}{\partial z} \right|_{z=0} = -w_0 \mathrm{e}^{\mathrm{i}(-\omega t + k_1 x + k_2 y)}, \quad x > hF(y). \tag{3}$$

The scattering problem is anti-symmetric across $z = 0$, therefore we also have

$$\phi_s|_{z=0} = 0, \quad x < hF(y). \tag{4}$$

This is a mixed boundary condition problem. The recent work from Ayton and Chaitanya [4] shows that this scattering problem can be solved using Wiener-Hopf method. For the sake of completeness we describe the essential steps as follows.

With the harmonic time dependence ($\phi_s = \Phi_s \mathrm{e}^{-\mathrm{i}\omega t}$), the convective wave equation becomes

$$\beta^2 \frac{\partial^2 \Phi_s}{\partial x^2} + \frac{\partial^2 \Phi_s}{\partial y^2} + \frac{\partial^2 \Phi_s}{\partial z^2} + 2\mathrm{i}kM \frac{\partial \Phi_s}{\partial x} + k^2 \Phi_s = 0, \tag{5}$$

where $\beta^2 = 1 - M^2$ and $k = k_1 M$. We emphasize again that the variables in equation (5) are non-dimensionalized as described above.

To eliminate the first-order differential term in equation (5), let a new dependent variable $\Phi = \Phi_s \mathrm{e}^{\mathrm{i}kMx/\beta^2}$. With the change of variable $\xi = [x - hF(y)]/\beta$, $\eta = y$ and $\zeta = z$, we have [4, 19]

$$\frac{\partial^2\Phi}{\partial\xi^2} + \frac{\partial^2\Phi}{\partial\eta^2} + \frac{\partial^2\Phi}{\partial\zeta^2} - 2\bar{h}F'(\eta)\frac{\partial^2\Phi}{\partial\xi\partial\eta} - \bar{h}F''(\eta)\frac{\partial\Phi}{\partial\xi} + \bar{h}^2F'^2(\eta)\frac{\partial^2\Phi}{\partial\xi^2} + \bar{k}^2\Phi = 0, \quad (6)$$

where $\bar{h} = h/\beta$ and $\bar{k} = k/\beta$. Upon defining $\bar{k}_1 = k_1/\beta$, we can show that the boundary conditions are now

$$\left.\frac{\partial\Phi}{\partial\zeta}\right|_{\zeta=0} = -w_0\mathrm{e}^{\mathrm{i}\left(\bar{k}_1\xi + \bar{k}_1\bar{h}F(\eta) + k_2\eta\right)}, \quad \xi > 0, \quad (7)$$

and

$$\Phi|_{\zeta=0} = 0, \quad \xi < 0. \quad (8)$$

Considering the spanwise periodicity of the serrations, we require that Φ also satisfies the following periodicity condition:

$$\Phi|_{\eta=0} = \Phi|_{\eta=1}\,\mathrm{e}^{-ik_2}, \quad \left.\frac{\partial\Phi}{\partial\eta}\right|_{\eta=0} = \left.\frac{\partial\Phi}{\partial\eta}\right|_{\eta=1}\mathrm{e}^{-ik_2}. \quad (9)$$

We can now perform Fourier Transformations in the streamwise direction, i.e.

$$\tilde{\Phi}(s,\eta,\zeta) = \int_{-\infty}^{\infty}\Phi(\xi,\eta,\zeta)\mathrm{e}^{\mathrm{i}s\xi}\mathrm{d}\xi. \quad (10)$$

Then it is straightforward to show that

$$(\bar{k}^2 - s^2)\tilde{\Phi} + \frac{\partial^2\tilde{\Phi}}{\partial\zeta^2} + \frac{\partial^2\tilde{\Phi}}{\partial\eta^2} + 2\mathrm{i}s\bar{h}F'(\eta)\frac{\partial\tilde{\Phi}}{\partial\eta} + \mathrm{i}s\bar{h}F''(\eta)\tilde{\Phi} - s^2\bar{h}^2F'(\eta)\tilde{\Phi} = 0. \quad (11)$$

Trying separable solutions $\tilde{\Phi}(s,\eta,\zeta) = Y(\eta;s)Z(\zeta;s)$ yields two ordinary differential equations [4]. Using the method of separation of variables, the general solution $\tilde{\Phi}$ can be written as

$$\tilde{\Phi}(s,\eta,\zeta) = \sum_{n=-\infty}^{\infty}A_n(s)\sum_{n=-\infty}^{\infty}A_n(s)\mathrm{sgn}(\zeta)\mathrm{e}^{-\gamma_n|\zeta|}\mathrm{e}^{-\mathrm{i}shF(\eta)}\mathrm{e}^{\mathrm{i}\chi_n\eta}, \quad (12)$$

where $\chi_n = 2n\pi + k_2$, $\gamma_n = \sqrt{s^2 - \kappa_n^2}$, $\kappa_n^2 = \bar{k}^2 - \chi_n^2$, $A_n(s)$ are analytical functions of the complex variable s and the sign function $\mathrm{sgn}(x)$ obtains 1 when $x \geq 0$ and -1 when $x < 0$. Because of the orthogonality of the functions $Y(\eta;s)$

with their Schwartz conjugates, each mode can be calculated individually using the Wiener-Hopf method (see Appendix A for details) to obtain

$$\tilde{\Phi}(s,\eta,\zeta)=\sum_{n=-\infty}^{\infty}\frac{\mathrm{i}w_0E_n(s)}{(s+\bar{k}_1)\sqrt{s+\kappa_n}\sqrt{-\bar{k}_1-\kappa_n}}\mathrm{sgn}(\zeta)\mathrm{e}^{-\gamma_n|\zeta|}\mathrm{e}^{-\mathrm{i}shF(\eta)}\mathrm{e}^{\mathrm{i}\chi_n\eta}, \tag{13}$$

where

$$E_n(s)=\int_0^1\mathrm{e}^{\mathrm{i}(\bar{k}_1+s)\bar{h}F(\eta)}\mathrm{e}^{-\mathrm{i}2n\pi\eta}\mathrm{d}\eta. \tag{14}$$

In the far-field, equation (13) can be inverse Fourier transformed using the method of stationary phase (see Appendix A) to be

$$\Phi(r,\theta,y)=\sum_{n=-\infty}^{\infty}\frac{\mathrm{e}^{\mathrm{i}\pi/4}}{\sqrt{\pi}}\frac{\mathrm{e}^{\mathrm{i}\kappa_n r}}{\sqrt{r}}\cos\frac{\theta}{2}\frac{w_0E_n(-\kappa_n\cos\theta)}{(-\kappa_n\cos\theta+\bar{k}_1)\sqrt{-\bar{k}_1-\kappa_n}}\mathrm{e}^{\mathrm{i}\chi_n y}. \tag{15}$$

Φ_s is directly given by $\Phi_s=\Phi\mathrm{e}^{-\mathrm{i}kMx/\beta^2}$ and the pressure is related to Φ_s via

$$p(r,\theta,y)=\mathrm{i}k_1\Phi_s-\frac{\partial\Phi_s}{\partial x}. \tag{16}$$

Equation (15) shows that the effects of serrations on velocity potential and the pressure are solely determined by the functions $E_n(-\kappa_n\cos\theta)$. Because at no other locations does the function $F(\eta)$ appear. This implies that one may be able to optimize the serration profile by studying the functions E_n, which will be shown in the rest of this paper. Equation (16) can be readily shown to be equivalent to

$$p(r,\theta,y)=\left(\mathrm{i}\frac{k_1}{\beta^2}\Phi-\frac{\partial\Phi}{\partial x}\right)\mathrm{e}^{-\mathrm{i}kMx/\beta^2}. \tag{17}$$

Equation (17) is still quite complicated. This is because equation (15) has a complicated dependence on the azimuthal angle θ, hence making the differentiation over x troublesome. However, considering that we are only interested in the far-field, we can greatly simplify the final results by only keeping the leading-order terms, i.e. ignoring the $r^{-3/2}$ and higher-order terms. This yields

$$p(r,\theta,y)\approx\sum_{n=-\infty}^{\infty}\mathrm{i}(\frac{k_1}{\beta^2}-\kappa_n\cos\theta)\frac{\mathrm{e}^{\mathrm{i}\pi/4}}{\sqrt{\pi}}\frac{\mathrm{e}^{\mathrm{i}\kappa_n r}}{\sqrt{r}}\cos\frac{\theta}{2}\frac{w_0E_n(-\kappa_n\cos\theta)\mathrm{e}^{-\mathrm{i}kMx/\beta^2}}{(-\kappa_n\cos\theta+\bar{k}_1)\sqrt{-\bar{k}_1-\kappa_n}}\mathrm{e}^{\mathrm{i}\chi_n y}. \tag{18}$$

To write equation (18) in a more compact form, let $H(\omega,\boldsymbol{x},k_2)$ denote

$$\frac{\mathrm{e}^{\mathrm{i}\pi/4}}{\sqrt{\pi}}\mathrm{e}^{-\mathrm{i}kMx/\beta^2}\cos\frac{\theta}{2}\sum_{n=-\infty}^{\infty}\frac{\frac{k_1}{\beta^2}-\kappa_n\cos\theta}{\bar{k}_1-\kappa_n\cos\theta}\frac{1}{\sqrt{\bar{k}_1+\kappa_n}}\frac{\mathrm{e}^{\mathrm{i}\kappa_n r}}{\sqrt{r}}\mathrm{e}^{\mathrm{i}\chi_n y}E_n(-\kappa_n\cos\theta). \tag{19}$$

Then equation (18) can be written in a more compact form as

$$p(r,\theta,y) \approx H(\omega,\boldsymbol{x},k_2)w_0 \tag{20}$$

Equation (18) is the induced far-field sound pressure by a single gust with a spanwise wavenumber k_2. The incoming turbulence can be modelled using a series of these gusts with different k_2 with a fixed value of $k_1 = \omega$, i.e.

$$w_t = \int_{-\infty}^{\infty} w_0(\omega,k_2)\mathrm{e}^{\mathrm{i}(-\omega t + k_1 x + k_2 y)}\mathrm{d}k_2. \tag{21}$$

Because of the linearity, the total sound pressure in the far-field induced by such turbulence, p_t, is given by

$$p_t(r,\theta,y) \approx \int_{-\infty}^{\infty} H(\omega,\boldsymbol{x},k_2)w_0(\omega,k_2)\mathrm{d}k_2. \tag{22}$$

3. Far-field sound power spectral density

Since the incoming turbulence is statistically stationary, the far-field sound is best formulated statistically. Routine procedure shows that the sound Power Spectral Density (PSD) of the far-field sound is given by

$$\Psi(\omega,r,\theta,y) = \lim_{T\to\infty}\frac{\pi}{T}p_t(r,\theta,y)p_t^*(r,\theta,y), \tag{23}$$

where $2T$ is the time interval used to performed temporal Fourier Transformation to obtain p_t and the asterisk denotes the complex conjugate. Substituting equations (22) into 23, we can show that

$$\Psi(\omega,r,\theta,y) \approx \int_{-\infty}^{\infty} |H(\omega,\boldsymbol{x},k_2)|^2\Phi_{ww}(\omega,k_2)\mathrm{d}k_2 \tag{24}$$

where $\Phi_{ww}(\omega,k_2)$ is the wavenumber power spectral density of the vertical velocity fluctuations defined by

$$\Phi_{ww}(\omega,k_2) = \lim_{T\to\infty}\frac{\pi}{T}w_0(\omega,k_2)w_0^*(\omega,k_2). \tag{25}$$

Writing $|H|^2$ explicitly, one obtains

$$|H(\omega,\boldsymbol{x},k_2)|^2 = \frac{1}{\pi}\cos^2\frac{\theta}{2}\left|\sum_{n=-\infty}^{\infty}\frac{\frac{k_1}{\beta^2}-\kappa_n\cos\theta}{\bar{k}_1-\kappa_n\cos\theta}\frac{1}{\sqrt{\bar{k}_1+\kappa_n}}\frac{\mathrm{e}^{\mathrm{i}\kappa_n r}}{\sqrt{r}}\mathrm{e}^{\mathrm{i}\chi_n y}E_n(-\kappa_n\cos\theta)\right|^2. \tag{26}$$

As mentioned in the preceding section, the effects of serrations profiles (for fixed serration wavelength and root-to-tip amplitudes) on the scattered sound are solely determined by the functions $E_n(-\kappa_n\cos\theta)$. Therefore, in the following section, we will focus on investigating the behaviour of $E_n(-\kappa_n\cos\theta)$ when the serration profiles change.

4. Optimizing serration geometries

Equation (24) gives the form of the far-field PSD at the azimuthal angle θ. To investigate the effects of serration shapes on far-field noise, it is convenient to restrict our attention to a specific observer point. We choose $\theta = \pi/2$ as a starting point, and we will see at the end of this section that the following analysis also holds for other observer angles. When $\theta = \pi/2$, equation (24) simplifies to

$$\Psi(\omega, r, \pi/2, y) \approx \frac{1}{\pi\beta^2}\cos^2\frac{\pi}{4}\int_{-\infty}^{\infty}\left|\sum_{-\infty}^{\infty}\frac{1}{\sqrt{\bar{k}_1+\kappa_n}}\frac{\mathrm{e}^{\mathrm{i}\kappa_n r}}{\sqrt{r}}\mathrm{e}^{\mathrm{i}\chi_n y}E_n(0)\right|^2\Phi_{ww}(\omega,k_2)\mathrm{d}k_2. \tag{27}$$

Equation (27) shows the sound reduction performance of the various serrations at $\theta = \pi/2$ is determined by the summation involving the functions $E_n(0)$, which do not depend on k_2.

From equation (46), we see

$$E_n(0) = \int_0^1 \mathrm{e}^{-\mathrm{i}2n\pi\eta}\mathrm{e}^{\mathrm{i}\bar{k}_1\bar{h}F(\eta)}\mathrm{d}\eta. \tag{28}$$

At low frequencies, we see that the exponent in the integral $\bar{k}_1\bar{h}F(\eta) \to 0$. Consequently, no matter what serration profile is used, $E_n(0) \to \delta_{n0}$, where δ_{nm} is the Kronecker delta. This is the same as that one would get for straight leading edges. Hence at low frequencies, virtually no sound reduction is possible, and the serration shape does not play any meaningful role as far as the leading-edge noise is concerned.

As the frequency increases, the exponent $\bar{k}_1\bar{h}F(\eta)$ varies from negative to positive values, and when this varying range is large enough, for example from $-\pi$ to π, the integrand (both real and imaginary parts) varies from negative to positive values. This results in oscillatory cancellation and the integrals obtain an amplitude of less than 1. However, in this intermediate frequency range, the serration shape plays a complicated role, and the exact optimal shape closely depends on which particular frequency we are more interested in. In general, therefore, it is unlikely to have one specific serration profile that outperforms any others in this entire frequency range.

Effective noise reduction can be achieved at relatively high frequencies, e.g. $\bar{k}_1\bar{h} > \pi$, where the oscillatory of the integrand becomes stronger and the cancellation becomes more effective. It is this frequency range that we are more interested in practical applications, which is also of our primary interest in this paper. To maximize the sound reduction at these relatively high frequencies,

we wish to start by minimizing $|E_n(0)|$ for each n as $\bar{k}_1\bar{h} \to \infty$. In the rest of this paper, we write the large number $\bar{k}_1\bar{h} = \Delta$ for clarity. Note here Δ simply denotes the non-dimensionalized hydrodynamic wavenumber (hence frequency) based on a half of the root-to-tip amplitude of the serration.

We categorise all possible single-valued serration shapes into those with stationary points, $F'(\eta) = 0$ for some η, and those without. In the following sections we consider the effects of stationary points on the value of $|E_n(0)|$. As we expect only a certain number of modes are cut-on in our frequency range of interest, we restrict our attention to finite $|n|$ values (which typically will be small, especially when the serration wavelength is small).

4.1. Serrations profiles with stationary points

Suppose $F(\eta)$ has stationary points at η_i, and for simplicity that $F''(\eta_i) \neq 0$. We may apply the standard Method of Stationary Phase [11] to (28) as $\Delta \to \infty$ by expanding the exponent of the integrand as

$$\mathrm{e}^{\mathrm{i}\Delta\left(F(\eta_i)+\frac{1}{2}F''(\eta_i)(\eta-\eta_i)^2+o((\eta-\eta_i)^3)\right)}. \tag{29}$$

Thus as $\Delta \to \infty$, (28) may be approximated by

$$E_n(0) \sim \sqrt{\frac{2\pi}{\Delta}} \sum_i \mathrm{e}^{-\mathrm{i}2n\pi\eta_i} \sqrt{\frac{1}{|F''(\eta_i)|}} \mathrm{e}^{\mathrm{i}\Delta F(\eta_i)} \mathrm{e}^{\mathrm{i}\mathrm{sgn}(F''(\eta_i))\frac{\pi}{4}}. \tag{30}$$

Note, if $F''(\eta_i) = 0$ for some i, the contribution from the ith stationary phase point would be larger than that given above, $O(\Delta^{-1/p})$, for p given by the order of the first non-zero derivative of F at η_i. This would correspond to retaining the first two non-zero terms in the expansion (29). We may therefore conclude that in the case of a serration profile with stationary points, $|E_n(0)| = O(1/\sqrt{\Delta})$ (or larger).

This may be understood from a physical perspective as follows. Recent work has shown that the primary noise reduction mechanism of using serrations on the leading- or trailing-edge of an aerofoil is due to the destructive interference [23, 19, 4]. Pressure phase variation is introduced on the serrated edge and leads to an effective cancellation. This can be seen clearly from equation (28), where the term $\mathrm{e}^{\mathrm{i}\Delta F(\eta)}$ oscillates rapidly when Δ is large. When $F(\eta)$ is everywhere-smooth, the main contribution of the integral shown in equation (28) comes from the region where $F(\eta)$ varies slowly, e.g. the stationary points. Hence the integral is determined by the small regions of stationary points in a way shown by equation (30).

For illustration purpose, we can take the serration profile $\sin(2\pi y)$ as an example. For this serration profile, we can evaluate analytically equation (28) to be

$$E_n(0) = J_n(\Delta), \tag{31}$$

where $J_n(z)$ is the nth-order Bessel function of the first kind. For large arguments, the Bessel function tends to

$$J_n(z) \sim \sqrt{\frac{2}{\pi z}} \cos\left(z - \frac{n\pi}{2} - \frac{\pi}{4}\right). \tag{32}$$

Hence we have

$$|E_n(0)| \sim \sqrt{\frac{2}{\pi\Delta}} \left|\cos\left(z - \frac{n\pi}{2} - \frac{\pi}{4}\right)\right|. \tag{33}$$

This is consistent with the results shown in equation (30).

4.2. Serration profiles without stationary points

We now suppose the serration profile does not have any stationary points. If the serration profile does not have stationary points then it cannot be everywhere smooth due to Rolle's theorem which states that any real-valued differentiable function that attains equal values at two distinct points must have at least one stationary point somewhere between them. Our real-valued serration function has $F(0) = F(1) = 0$, thus to not have any stationary points, it must not be formally differentiable for all points $\eta \in [0, 1]$ (for a function to be formally differentiable we require that its derivative never has a jump discontinuity, thus for example a sawtooth is not formally differentiable at its tip or root).

Suppose $F(\eta)$ is not formally differentiable at points $\tilde{\eta}_i$, ordered such that $\tilde{\eta}_0 < \tilde{\eta}_1 < \ldots$. Between neighbouring points, we may assume our function is continuous and differentiable. We may therefore separate our integral over $[0, 1]$, (28), to integrals over, $[0, \tilde{\eta}_0]$, $[\tilde{\eta}_0, \tilde{\eta}_1], \ldots$. We may integrate by parts each sub-region to obtain

$$E_n(0) = \sum_i \frac{1}{\mathrm{i}\Delta} \left(\frac{\mathrm{e}^{-\mathrm{i}2n\pi\eta}\mathrm{e}^{\mathrm{i}\Delta F(\eta)}}{F'(\eta)}\bigg|_{\tilde{\eta}_i}^{\tilde{\eta}_{i+1}} - \int_{\tilde{\eta}_i}^{\tilde{\eta}_{i+1}} \mathrm{e}^{\mathrm{i}\Delta F(\eta)} \frac{\mathrm{d}}{\mathrm{d}\eta} \frac{\mathrm{e}^{-\mathrm{i}2n\pi\eta}}{F'(\eta)} \mathrm{d}\eta \right). \tag{34}$$

By the Riemann-Lebesgue lemma, the second term in the above expression is $o(1)$ as $\Delta \to \infty$, thus

$$E_n(0) \sim \frac{1}{\mathrm{i}\Delta} \sum_i \frac{\mathrm{e}^{-\mathrm{i}2n\pi\eta}\mathrm{e}^{\mathrm{i}\Delta F(\eta)}}{F'(\eta)}\bigg|_{\tilde{\eta}_i}^{\tilde{\eta}_{i+1}}, \tag{35}$$

which is $O(1/\Delta)$. This is much smaller than the contribution in equation (30) for serrations with stationary points.

Hence to have a better noise reduction performance at high frequencies, we prefer serration profiles without stationary points.

Equation (35) however tells us more information than just that described above. In particular, it shows that the asymptotic value of $|E_n(0)|$ depends crucially on the slope of the serration profile at the non-smooth points. It is not very sensitive on the slope at other points. More importantly this shows that the larger the absolute value of $F'(\tilde{\eta}_i)$ is, the smaller each term's magnitude in the sum shown in equation (35) is. Therefore, to minimize $|E_n(0)|$, it is desirable to have a serration shape that is sharper (large slope magnitude) in the local vicinity around the non-smooth points. For a sawtooth serration profile that is commonly used in various application, the slope magnitude is uniformly the same as 4. However, by using a serration that is sharper at the non-smooth points, for example, with the slope magnitude being 8, we would expect a further noise reduction by around 6 dB.

The results obtained so far may be understood from a physical perspective as follows. From equation (28), when $F(\eta)$ is piecewise smooth and contains no stationary points, the contribution of integral mainly comes from the end points, where cancellation is hindered by the abrupt termination of the interval. To understand the preference of sharper non-smooth points, an illustration is shown in figure 2. Two serration profiles are shown in this figure. The left profile is sharper at the non-smooth points whereas the right one is less so. In both serration profiles, the spanwise (η) regions which contribute most to the integral are illustrated by two vertical lines. The regions outside contribute little to the integral because of effective cancellation due to the phase variation of the pressure on the serrated edge. This can happen for example when an integral number of wavelengths of a plane-wave-like pressure gust are fitted within this region. Now, compared to the contribution region for the left serration profile, it is clear that the spanwise distance of the contribution region for the right serration is much wider. Therefore the integral would obtain a large amplitude (a large value of $\mathrm{d}\eta$ in equation (28)). This explains why sharper non-smooth points are desirable.

But one should bear in mind that these results are obtained for high frequencies. Therefore, in the intermediate frequency regime, e.g. $\bar{k}_1\bar{h} < \pi$, we may see a decrease of the noise reduction performance. In fact, we somewhat expect this to happen. Compared with the sawtooth serration with uniform slope magnitude, changing the slope distribution causes the phase patterns along the edge to be less uniform, resulting in a less effective destructive interference at relatively low frequencies, hence a poorer noise reduction performance. For ex-

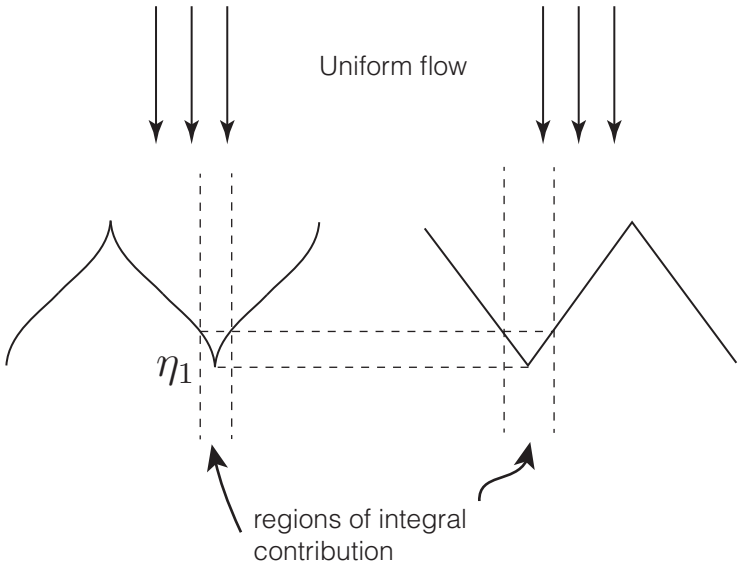

Figure 2: Comparison of the integral contribution regions for two different serrations profiles: left) sharp non-smooth points; right) less-sharp non-smooth points.

ample, when Δ takes an intermediate value of π, we expect a perfect destructive interference to occur on the edge of a sawtooth serration, hence a large noise reduction around this frequency. On the other hand, at the same frequency, due to the non-linear variation of $F(\eta)$ for the new serration type, a perfect cancellation is not possible, and hence a poorer noise reduction. However, as frequency increases, the advantage of this new type of serration will quickly overtake.

Although the above asymptotic analysis is based on one observer point at $\theta = \pi/2$, it can be shown that it also serves as a good approximation at other θ values as follows. Consider

$$E_n(-\kappa_n \cos\theta) = \int_0^1 \mathrm{e}^{\mathrm{i}(\bar{k}_1 - \kappa_n \cos\theta)\bar{h}F(\eta)} \mathrm{e}^{-\mathrm{i}2n\pi\eta} \mathrm{d}\eta. \tag{36}$$

We only need to replace $\Delta = (\bar{k}_1 - \kappa_n \cos\theta)h$ and the previous asymptotic analysis would still hold, because we are only interested in the cut-on modes where κ_n is a real number less than $\bar{k}$.

5. An illustrative design

With the results shown in section 2 in mind, we propose one of this kind of serration profiles as an example, which is given by

$$F(\eta) = \begin{cases} \dfrac{1}{\tan b/4} \tan(b\eta), & 0 \le \eta < 1/4, \\ \dfrac{1}{\tan b/4} \tan(b(-\eta + \dfrac{1}{2}), & 1/4 \le \eta < 3/4, \\ \dfrac{1}{\tan b/4} \tan(b(\eta - 1)), & 3/4 \le \eta \le 1, \end{cases} \tag{37}$$

where b is a non-negative number quantifying how sharp the serration is at the non-smooth points. For example, when $b \to 0$, the serration reduces to the sawtooth serration. When $b \to 2\pi$, the slope at the non-smooth points approaches infinity. Note we should avoid this case, since when $b \to 2\pi$, the slope near $\eta = 0$ approaches 0, i.e. $\eta = 0$ tends to a stationary point which we have classified as non-ideal. An intermediate value is desirable, for example, $b = 1.5\pi$. Profiles of different b values are shown in figure 3. It can be seen that when $b = 1.8\pi$, the profile becomes highly non-uniform – in particular, the slope at the non-smooth points is very large and at $\eta = 0$ is close to 0. Note that the $\tan(x)$ function shown in equation (37) represents only one possible form for the serration profile and is chosen for illustration purposes. Other function forms would also work.

5.1. The behaviour of the functions E_n

To illustrate the potential advantage of using the new type of serration, we plot $10 \log 10 |E_0(0)|^2$ in figure 4. We can see that as $\Delta \to \infty$, the value of $|E_0|$ does indeed decay more quickly compared to that for the sawtooth serration. The extra noise reduction is up to 10 dB. As another illustration, we plot the $10 \log 10 |E_2(0)|^2$ in figure 5. Comparing with figure 4, it seems that the compromised frequency regime starts to shift to a higher frequency. Indeed, this can be shown to be generally true when the mode number n increases. However, in practical applications, the serration wavelength is small, therefore the nth-order mode are cut-on only when k_2 is close to $-2n\pi$. But when k_2 becomes large, the incoming turbulent wavenumber spectrum decays. Hence only a finite number of modes N are practically needed in the frequency range of interest and N decreases as the frequency decreases. As a fixed frequency, it can be shown that N decreases when the serration wavelength decreases from, for example, the spectrum model shown in the following section. Consequently, to

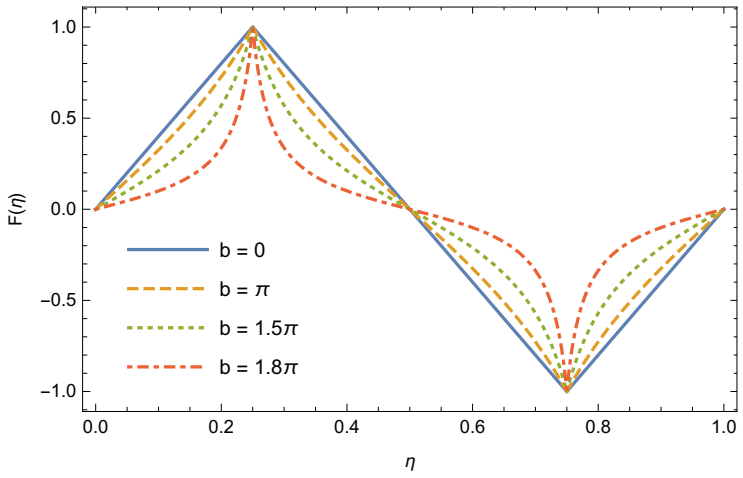

Figure 3: The serration profiles of the newly proposed serration with different values of b. When $b = 0$, the profile reduces to a sawtooth one. When $h \to 2\pi$ the serration becomes highly non-uniform with the slope at the non-smooth points approaches to infinity and the point $\eta = 0$ approaches to a stationary point.

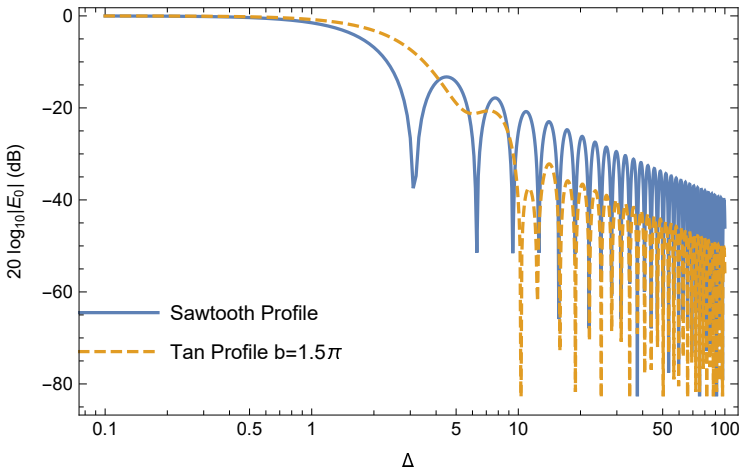

Figure 4: Comparison of the decay rates of $|E_0|$ for sawtooth and the new illustrative serration as the frequency increases. $|E_0|$ decays faster for the new design at high frequency with a narrow compromised low frequency range.

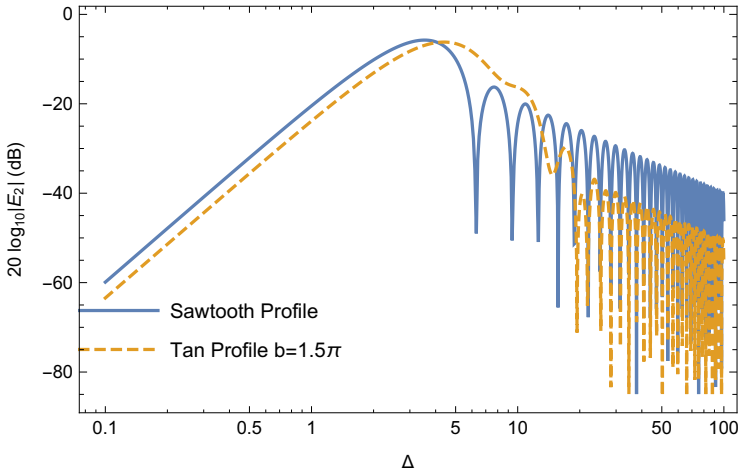

Figure 5: Comparison of the decay rates of $|E_2|$ for sawtooth and the new type of serration as the frequency increases. The compromised region moves to higher frequencies.

maximize the noise reduction benefit, a small serration wavelength is desirable. This will be further demonstrated in the following section. It should be noted that when the frequency is extremely high, the number of cut-on modes N might be large enough such that the additional advantage of using this new serration is buried by the compromised modes. However, in practical applications, sound intensity at these extremely large frequencies is often negligible, consequently we are only interested in the intermediate-to-high frequency range ($\pi < k_1 h < 100$ for example) where the benefits do exist. The high end of the frequency range where an improved acoustic performance is possible depends on how quickly the turbulent spectrum decays with k_2. We will discuss the spectrum in detail in the following section.

5.2. The overall noise reduction

Section 5.1 shows that the new type of serration does result in a reduced value of $|E_n(0)|^2$ at high frequencies. However because there are multiple cut-on modes, it is still not clear exactly how much additional benefit can be expected by using the new type of serration and what the most effective frequency range is. In this section, we predict the overall benefit by using a realistic wavenumber spectrum to model the incoming turbulence.

There are many empirical models for the incoming turbulent spectrum available. As an illustration, we use the one developed from Von Kármàn spectrum. Based on this, it can be shown that Φ_{ww}, which is the energy spectrum of the

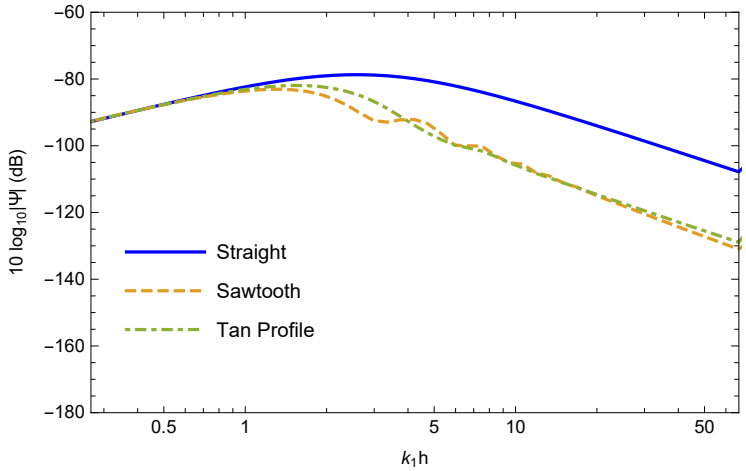

Figure 6: The predicted far-field PSD for flat plates with straight edge, sawtooth and the illustrative serration ($b = 1.4\pi$) respectively when $h = 2$, i.e. for wide serrations.

incoming vertical fluctuation velocity, can be written as [1, 22, 19]

$$\Phi_{ww}(\omega, k_2) = \frac{4\mathrm{TI}^2}{9\pi k_e^2} \frac{\hat{k}_1^2 + \hat{k}_2^2}{(1 + \hat{k}_1^2 + \hat{k}_2^2)^{7/3}}, \tag{38}$$

where TI denotes the turbulent intensity and k_e, $\hat{k}_1$ and $\hat{k}_2$ are given by

$$k_e = \frac{\sqrt{\pi}\Gamma(5/6)}{L_t\Gamma(1/3)}, \quad \hat{k}_1 = \frac{k_1}{k_e}, \quad \hat{k}_2 = \frac{k_2}{k_e}. \tag{39}$$

In the above equations, L_t is the integral scale of the turbulence (also normalised by the serration wavelength) and $\Gamma(x)$ is the Gamma function.

In order to put equation (38) into perspective, we need to have a realistic set of physical parameters for the incoming flow. For convenience, we use those in the previous experiment [27, 19], i.e. $M = 0.18$ and $\mathrm{TI} = 0.025$. In order to show the effects of serration wavelength, we fix the dimensional serration amplitude and the dimensional turbulence integral scale and only vary the value of dimensional serration wavelength. This implies that the non-dimensional numbers h varying from 2 to 10 and L_t varying from 0.5 to 2.5. In the rest of this section, the observer location is fixed at $r = 30$, $\theta = \pi/2$ and $y = 0$ and the far-field PSDs are evaluated from equation (27).

Figure 6 shows the far-field PSDs for flat plates with straight edge, sawtooth and the illustrative serrations of $h = 2$ and $b = 1.4\pi$, respectively. This results in quiet wide serrations. As discussed in section 5.1, wide serrations imply that more modes need to be considered. Consequently, the additional benefit may

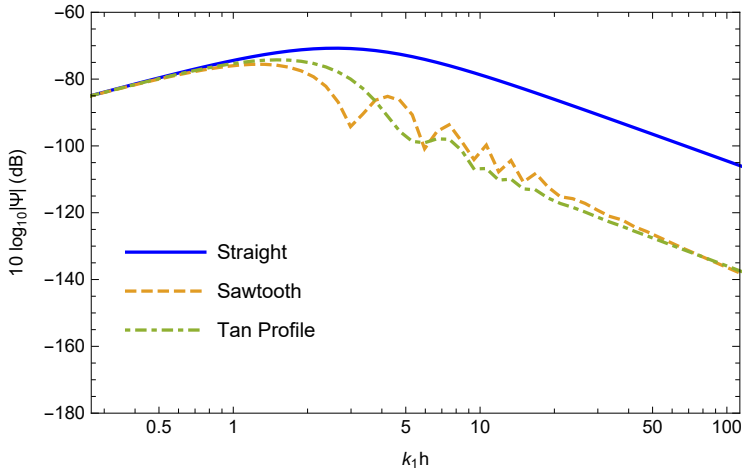

Figure 7: The predicted far-field PSD for flat plates with straight edge, sawtooth and the illustrative serration ($b = 1.4\pi$) respectively when $h = 5$, i.e. for sharp serrations.

not be obtained due to the inclusion of high-order modes. This is in accord with the results shown in figure 6, where the advantage is negligible in the frequency range of interest. There is also a slight but negligible noise increase in the high-frequency regime compared to the sawtooth serrations, which, as we discussed in section 5.1, could occur due to the inclusion of many high-order modes. However, it is worth noting that if we decrease the value of b, i.e. we decrease the maximum benefit we can expect, advantages of using this new serration may be more pronounced. In either case, however, the benefit of using such a new type of serration is not significant at these parameters.

In order to allow an improved sound reduction to occur in the frequency range of interest, we need to use sharper serrations. When the serration amplitude is fixed a small serration wavelength implies a large h. Figure 7 shows the results when $h = 5$. Compared to figure 6, the benefit of using the illustrative profile starts to appear at $k_1 h \approx 4$ and last until $k_1 h \approx 100$. An extra 4 dB is achieved compared to the traditional sawtooth serration in the intermediate frequency range. It is worth noting that the predicted spectrum starts to oscillate. This is because when the serration wavelength is small, the far-field sound is dominated by mode 0. The peaks and troughs are due to the behaviour of $E_0(0)$.

A larger acoustic benefit can be obtained for even sharper serrations. This is shown in figure 8, where $h \approx 10$. A nearly uniform 8 dB extra reduction is accomplished by using the new design when $5 < k_1 h < 50$. When the frequency

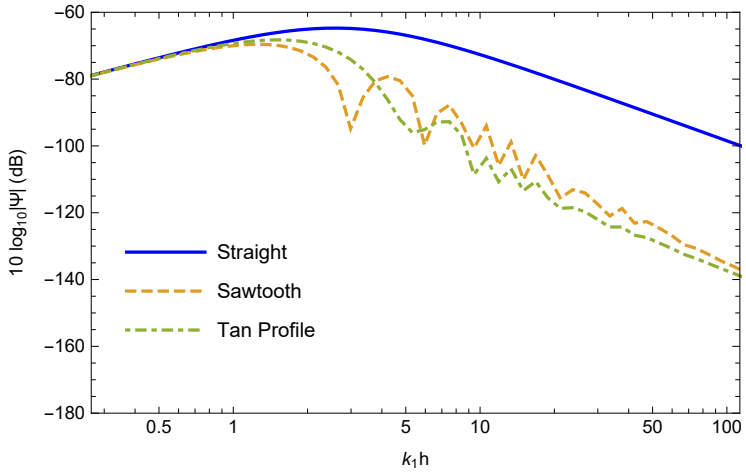

Figure 8: The predicted far-field PSD for flat plates with straight edge, sawtooth and the illustrative serration ($b = 1.4\pi$) respectively when $h = 10$, i.e. very sharp serrations.

is higher than $k_1 h = 50$, the benefit of using the new serration starts to diminish. As mentioned in the preceding section, this is due to the fact that more modes are now cut-on and the advantage is limited by the compromised modes. Comparing Figures 6 to 8, we can find that $k_1 h$, or $\bar{k}_1 \bar{h}$ to be more precise, is the correct non-dimensional quantity characterizing the noise reduction effects of serrations. This is evident from equation (28) and in agreement with our earlier findings [19].

To show how the additional noise reduction benefit by using the new serration profile depends on the observer angle, we also compare the noise directivity patterns for the sawtooth and new serrations. We choose the same set of parameters as those used in figure 8. Results are shown in figure 9, where we have plotted $10\log_{10}(\Psi) + 150$ instead of $10\log_{10}(\Psi)$ to avoid negative decibel values. Figure 9(a) is at a low frequency of $k_1 h = 0.5$. As we can see, both the sawtooth and new serrations result in little noise reduction compare to straight leading edges. This is consistent with the results shown in figures 6 to 8. As the frequency increases to $k_1 h = 4$, the directivity patterns change to that shown in figure 9(b). At this frequency, additional noise reduction benefit is achieved for observer angles in the range of 80° and 280°. The slight noise increase observed at small observer angles is, as mentioned above, due to the low-frequency penalty, as shown in figure 8. As the frequency increases to $k_1 h = 15$, the directivity patterns change to those shown in figure 9(c). It is clear that additional noise reduction due to the use of new serrations is achieved

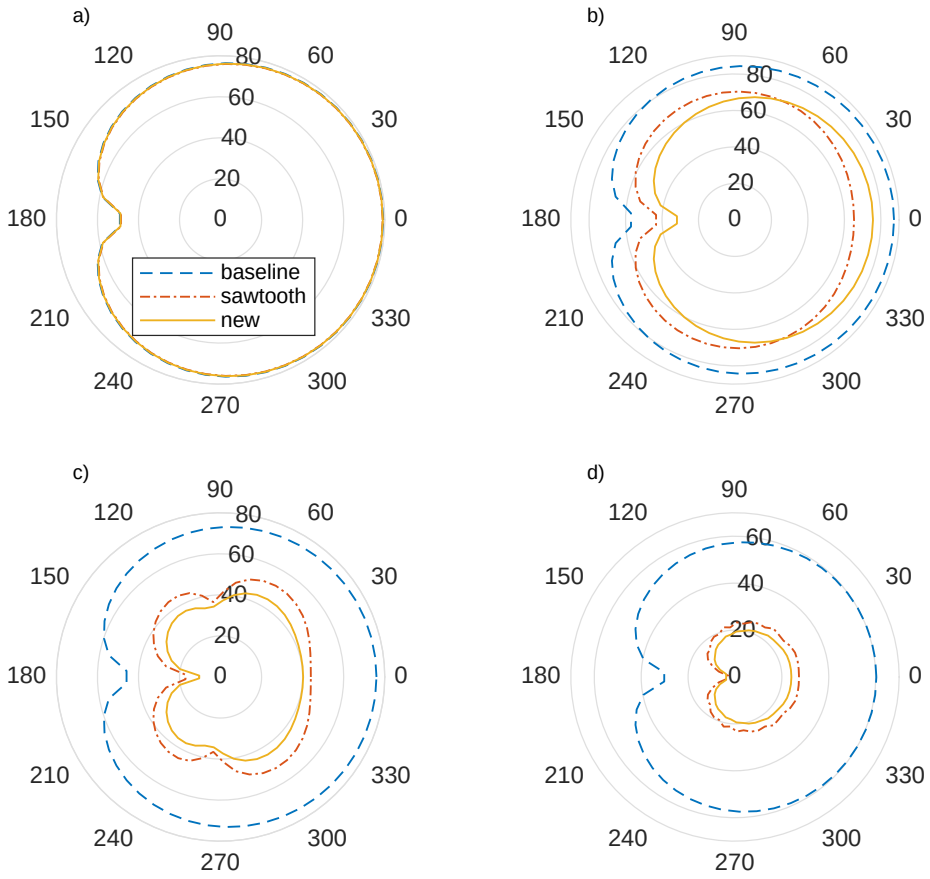

Figure 9: Comparison of the noise directivity patterns in dB ($10\log_{10}(\Psi)+150$) for serrations of the sawtooth and new profiles: a) $k_1h = 0.5$; b) $k_1h = 4$; c) $k_1h = 15$; d) $k_1h = 60$.

at all observer angles. It is this frequency range that we mainly focused on and discussed in detail in figures 6 to 8. As the frequency increases to an even larger value of $k_1h = 60$, the additional benefit starts to drop slightly, but extra noise reduction is achieved at all observer angles, as shown in figure 9(d).

In summary, the proposed illustrative design does result in a better noise reduction performance in the frequency range of interest, and the extra noise reduction due to the use of new serrations is achieved at all observer angles in this frequency range. However, in order to gain the full advantage of the new design, the serration must be sufficiently sharp. The low-frequency increase caused by using the new design is largely negligible. In this paper, we focus on the acoustic effects of leading-edge serrations. But it is worth noting that previous research has shown that the use of leading-edge serrations may lead to a slight

(a) The experimental rig was placed in the aeroacoustic wind tunnel. The flat plate was placed near the exit of the wind tunnel and a microphone arc was suspended above the aerofoil to measure the far-field noise.

(b) The serrated leading edge was formed by joining the serration insert and the flat plate together. The serration insert was cut according to equation (37) and the parameter b was varied between 0, π, 1.2π and 1.5π.

Figure 10: Photographs of the wind tunnel, the microphone arc and the flat plate with a serrated leading edge.

aerodynamic penalty at a small angle of attack but can also significantly improve the lift coefficient at large angles of attack and notably postpone aerodynamic stall [37, 13, 24, 28, 15, 30]. We expect similar aerodynamic effects by using the new serration proposed in this paper.

6. Experimental validation

Section 5 shows that the use of the new serration profile can provide up to 8 dB more noise reduction in the high frequency range without severely affecting the low-frequency performance. In this section, we wish to experimentally verify such a conclusion.

6.1. Experimental setup

The experiment was carried out in the aeroacoustic facility in the University of Southampton; a photograph of the rig is shown in figure 10a. The experimental rig was placed inside the anechoic chamber of dimensions 8 m $\times$ 8 m $\times$ 8 m. The anechoic chamber has a cut-off frequency around 80 Hz. The low-speed wind tunnel can go up to a Mach number around 0.3. In the experiment, the jet velocities were varied between 20, 40, 60 and 80 m/s. The exit of the wind tunnel has a dimension of 150 mm $\times$ 450 mm.

A number of flat plates with a mean chord length 150 mm and span 450 mm were placed at 150 mm downstream of the wind tunnel exit. The flat plates were constructed by joining together two 1 mm thick metallic sheets to allow serrated

flat-plate inserts to be inserted between them. All corners of the plates were rounded and the trailing edge was sharpened to eliminate vortex shedding noise. The work of Narayanan et al. [27] contained more details on the construction of these flat plates. The flat plates used in the experiment included those with a straight leading edge and serrated leading edges of various profile parameters by varying b and h. The serration wavelength was also varied independently. To prevent tonal noise generation observed in the laminar boundary layer [29, 34], the flow near the leading edge of the flat plate was tripped on both the pressure and suction sides to force transition to turbulence using a rough band of tape. The tape had a width of 1.25 cm and was located at 16.6% of the chord from the leading edge. The tape had roughness of SS 100, corresponding to a surface roughness of 140 µm. Previous noise measurements in this facility have indicated that self-noise is insensitive to this type of tripping.

A microphone arc was placed above the aerofoil to measure the far-field noise at different angles in the mid-span plane. The microphone arc has 11, 1.27 cm condenser microphones (B&K type 4189) located at a constant radial distance of 1.2 m from the leading edge of the flat plate, spanning an observer angle from 40° to 140° measured relative to the downstream jet axis. Noise measurements were carried out for 10 s at a sample frequency of 50 kHz. The noise spectra were calculated with a window size of 1024 data points corresponding to a frequency resolution of 48.83 Hz and a BT product of approximately 500 , which is sufficient to ensure negligible variance in the spectral estimate at this frequency resolution. The noise spectra are presented in terms of the Sound Power Level (PWL) and Sound Pressure Level (SPL) using the procedure described by Narayanan et al. [27], i.e. the PWL is calculated by integrating the sound power spectral density over an observer angle range between 40° and 140° in the mid-span plane (equations (3) and (4) in Narayanan et al. [27]).

6.2. Turbulence spectra

A bi-planar rectangular grid with overall dimensions of 630 mm × 690 mm was used to generate nearly homogeneous turbulence. The grid was located in the contraction section of the wind tunnel at 75 cm upstream the nozzle exit. Turbulence generated using this grid provided a velocity spectrum at the leading edge of the plate that is a close approximation to that due to homogeneous and isotropic turbulence, the energy spectrum of which is known to be well modelled by a number of empirical formula. We use the aforementioned one based on the Von Kármàn spectrum to model the energy spectrum for the vertical fluctuation velocity. Previous studies have shown that this model can

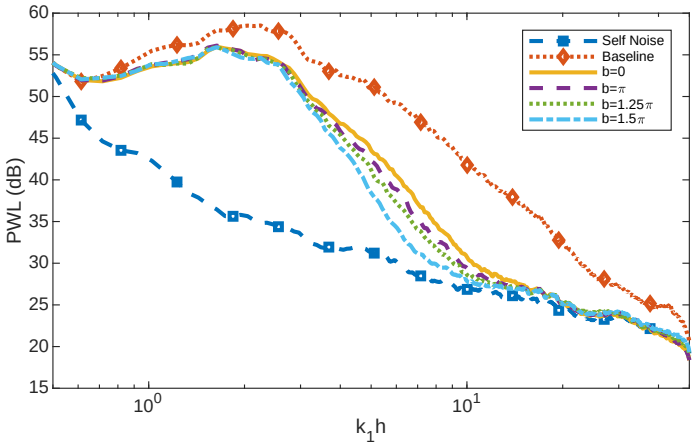

Figure 11: The far-field PWL spectra of the leading-edge noise for the baseline and serrated flat plates. The serrations have a fixed wavelength 5 mm and half tip-to-root amplitude 25 mm. Also included is the spectrum for the flat plate's self-noise, where no grid turbulence is present.

agree with experiments excellently (see for example Narayanan et al. [27]). In this experiment, the turbulence intensity was around 2.5% and the streamwise integral length-scale was around 6 mm.

6.3. Far-field sound spectra

The far-field sound spectra are presented using the PWL. PWL is defined to describe the sound power spectral density integrated over the observer angle. A detailed definition of PWL is given by equation 4 of Narayanan et al. [27].

The first test case is for serrations with a wavelength 5 mm and half root-to-tip amplitude 25 mm, corresponding to $h = 5$, at a jet velocity 60 m/s. The value of b is varied between 0, π, 1.2π and 1.5π, respectively. Also included are the baseline test, where no serration is used, and the self-noise test, where the serration of $b = 1.5\pi$ is used without grid turbulence. The results are shown in figure 11. The self-noise spectrum is shown by the dashed line. We can see that from the frequency $k_1 h \approx 0.5$ to 10 the leading-edge noise from the baseline test case is at least 15 dB higher than the self-noise. We can therefore confidently regard the measured noise as due to the interaction between the leading edge and grid turbulence in this frequency range. As the frequency increases, care must be taken as the self-noise becomes more and more important, and in particular, when leading-edge noise is reduced significantly by using serrations, the total noise would be dominated by the self-noise. The self-noise consists of a number of sources, including the turbulent boundary layer trailing-edge (TE)

noise [21, 20], flat plate tip noise and so on, among which TE noise is likely to be dominant.

As mentioned in section 5, $b = 0$ implies that the serration reduces to a conventional sawtooth profile. Figure 11 shows that the use of the conventional sawtooth serration leads to significant noise reduction in the frequency range $k_1 h > 1$, which is consistent with numerous earlier findings. However, we are more interested to see whether a greater reduction can be achieved by using the new serration profile with $b > 0$. Figure 11 demonstrates that this indeed can be achieved. For example, for the case where $b = 1.5\pi$, an additional sound reduction up to 7 dB is observed in the experiment with little effect on the low-frequency performance. This is remarkable since we have in essence achieved an additional 7 dB sound reduction by simply changing the serration geometry, without paying observable prices. The additional benefit vanishes for frequencies larger than $k_1 h = 20$. This is because the self-noise mechanisms, such as the aforementioned TE noise, start to dominant. Hence, although the leading-edge noise is reduced more effectively, this is hidden by the dominance of TE noise. Figure 11 also confirms that the larger b is, the more benefit can be expected. For instance, for $b = \pi$, 1.25π and 1.5π, the additional reduction is around 2 dB, 3 dB and 7 dB, respectively. This has been predicted in sections 4 and 5.

The second test case is for a serration wavelength 5 mm and half root-to-tip amplitude $\tilde{h} = 12$ mm. This corresponds to the value $h = 2.4$. The results are shown in figure 12. Due to a smaller value of h, the effective (where the self-noise is negligible) non-dimensional frequency ($k_1 h$) range is now shifted to a lower regime. Also it can be seen that the maximum additional benefit in the frequency range of interest is around 4 dB. This is consistent with our earlier conclusions, i.e. in order to achieve great benefit in the frequency range of interest, the serration must be sufficiently sharp (large h).

In both test cases, however, it is worth mentioning that the use of the new serrations also results in an additional reduction of the aerofoil self-noise compared to conventional sawtooth serrations. This is important, because it shows that the use of the new serration can indeed provide additional noise reduction benefit without in any way jeopardising its performance by other source components.

7. Conclusion and future work

Based on an analytical model of the leading-edge noise due to serrated leading edges of arbitrary shapes, this paper explores the acoustic optimality of

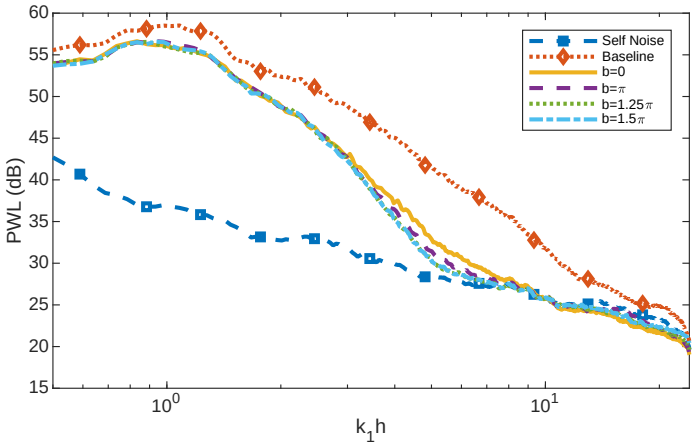

Figure 12: The far-field PWL spectra of the leading-edge noise for the baseline and serrated flat plates. The serrations have a fixed wavelength 5 mm and half tip-to-root amplitude 12 mm. Also included is the spectrum for the flat plate's self-noise, where no grid turbulence is present.

different serration profiles. An asymptotic analysis is performed to investigate the effects of serrations geometry on high-frequency leading-edge noise reduction.

It is found that in order to accomplish the best sound reduction performance at high frequencies, the serration profile cannot have any stationary points. The piecewise smooth functions can be constructed to satisfy this condition. For such serrations, improved noise reduction performance may be obtained for serrations with large slopes at the non-smooth points compared to the widely used sawtooth serrations. This requires that the serration profile is not uniform (linear) any more. An illustrative design is proposed as an example.

To study the exact benefit one may obtain by using the new design in practical applications, an energy spectrum for the vertical velocity fluctuations of the incoming turbulence based on the Von Kármàn spectrum is used. The predicted PSDs at 90° above the serration are compared with those for the widely used sawtooth serrations. It is found that additional noise reduction, up to 8 dB for example, can be achieved in the frequency range of interest with sufficiently sharp serrations. A comparison of noise directivity patterns shows that that this additional noise reduction is achieved at all observer angles in this frequency range.At low frequencies, one may expect a slight noise increase but this is often negligible. Following the analytical prediction, an experimental investigation was carried out. The experimental results show that the new design is indeed superior than the conventional sawtooth design. For example, a

remarkable 7 dB additional noise reduction was observed using one of the new type of serrations compared with conventional sawtooth serration. The trends predicted in the analytical section are well supported by the experiment. The current study focuses on the leading-edge noise and its reduction using leading-edge serrations. However, the noise reduction mechanism is known to be similar to that for the turbulent boundary layer trailing-edge noise. Hence, the present analysis and newly proposed serration profile are expected to work in a similar manner for the TE problem. This forms part of our future work.

Acknowledgement

The authors wish to gratefully acknowledge the financial support provided by the EPSRC under the grant number EP/P015980/1.

Appendix A

Wiener-Hopf procedure

The Wiener-Hopf procedure can be performed as follows. First, when $\zeta = 0$ one has

$$\tilde{\Phi}'(s,\eta,\zeta)\Big|_{\zeta=0} = \sum_{n=-\infty}^{\infty} -\gamma_n A_n(s) \mathrm{e}^{-\mathrm{i}shF(\eta)} \mathrm{e}^{\mathrm{i}\chi_n \eta}, \tag{40}$$

and

$$\tilde{\Phi}(s,\eta,\zeta)|_{\zeta=0} = \sum_{n=-\infty}^{\infty} A_n(s) \mathrm{e}^{-\mathrm{i}shF(\eta)} \mathrm{e}^{\mathrm{i}\chi_n \eta}, \tag{41}$$

where, we have defined $\tilde{\Phi}' = \partial\tilde{\Phi}/\partial\zeta$ for simplicity.

On the other hand, from the boundary conditions, equations (7) and (8), one obtains

$$\tilde{\Phi}'(s,\eta,\zeta)\Big|_{\zeta=0} = \frac{w_0}{\mathrm{i}(s+\bar{k}_1)} \mathrm{e}^{\mathrm{i}\bar{k}_1 \bar{h} F(\eta) + k_2 \eta} + \tilde{\Phi}'_-, \tag{42}$$

and

$$\tilde{\Phi}\Big|_{\zeta=0} = \tilde{\Phi}_+, \tag{43}$$

where the $+$ and $-$ subscripts indicate that the corresponding functions are analytic in the upper and lower s planes, respectively.

Comparing equations (40) and (42) and equations (41) and (43), one can show that

$$-\gamma_n A_n(s) = \frac{w_0}{\mathrm{i}(s+\bar{k}_1)} E_n(s) + \tilde{\Phi}'_{n-}, \tag{44}$$

and

$$A_n(s) = \tilde{\Phi}_{n+}, \tag{45}$$

where

$$E_n(s) = \int_0^1 \mathrm{e}^{\mathrm{i}(\bar{k}_1+s)\bar{h}F(\eta)}\mathrm{e}^{-\mathrm{i}2n\pi\eta}\mathrm{d}\eta. \tag{46}$$

The functions $\tilde{\Phi}'_{n-}$ and $\tilde{\Phi}_{n+}$ are defined in a similar manner and still preserve their analyticity in their own half planes. Combining equations (44) and (45), we obtain

$$\gamma_n\tilde{\Phi}_{n+} + \tilde{\Phi}'_{n-} = \frac{-w_0}{\mathrm{i}(s+\bar{k}_1)}E_n(s). \tag{47}$$

The kernel decomposition is standard, using which equation (47) can be written as

$$\begin{aligned}&\sqrt{s+\kappa_n}\tilde{\Phi}_{n+} + \frac{\tilde{\Phi}'_{n-}}{\sqrt{s-\kappa_n}}\\ &= -w_0E_n(s)\left[\frac{1}{\mathrm{i}(s+\bar{k}_1)\sqrt{s-\kappa_n}} - \frac{1}{\mathrm{i}(s+\bar{k}_1)\sqrt{-\bar{k}_1-\kappa_n}}\right] - \frac{w_0E_n(s)}{\mathrm{i}(s+\bar{k}_1)\sqrt{-\bar{k}_1-\kappa_n}}.\end{aligned} \tag{48}$$

Routine procedure [4] yields

$$A_n(s) = \tilde{\Phi}_{n+} = \frac{\mathrm{i}w_0E_n(s)}{(s+\bar{k}_1)\sqrt{s+\kappa_n}\sqrt{-\bar{k}_1-\kappa_n}}. \tag{49}$$

Substituting equation (49) to equation (12), we have

$$\tilde{\Phi}(s,\eta,\zeta) = \sum_{n=-\infty}^{\infty}\frac{\mathrm{i}w_0E_n(s)}{(s+\bar{k}_1)\sqrt{s+\kappa_n}\sqrt{-\bar{k}_1-\kappa_n}}\mathrm{sgn}(\zeta)\mathrm{e}^{-\gamma_n|\zeta|}\mathrm{e}^{-\mathrm{i}shF(\eta)}\mathrm{e}^{\mathrm{i}\chi_n\eta}. \tag{50}$$

Method of stationary phase

In the far-field, equation (50) can be inverse Fourier transformed using the method of stationary phase as follows. When the κ_n is real, such as when $n = 0$, we invert the Fourier transform in the far-field with the deformed path shown in figure 13. When κ_n is imaginary, we deformed the integral path to that shown in figure 14. In both figures, the dashed paths Σ_1 and Σ_3 are arcs of a large radius R. It can be shown that the integral over path segments Σ_1 and Σ_3 vanish when $R \to \infty$. The path segment Σ_2 are hyperbolas given by

$$s = -\kappa_n\cosh(\mathrm{i}\theta + t), \tag{51}$$

where the real argument t ranges from $-\infty$ to ∞ and θ is defined as the azimuthal angle in the $x-z$ plane, i.e.

$$x = \xi + hF(\eta) = r\cos\theta, \quad z = r\sin\theta, \tag{52}$$

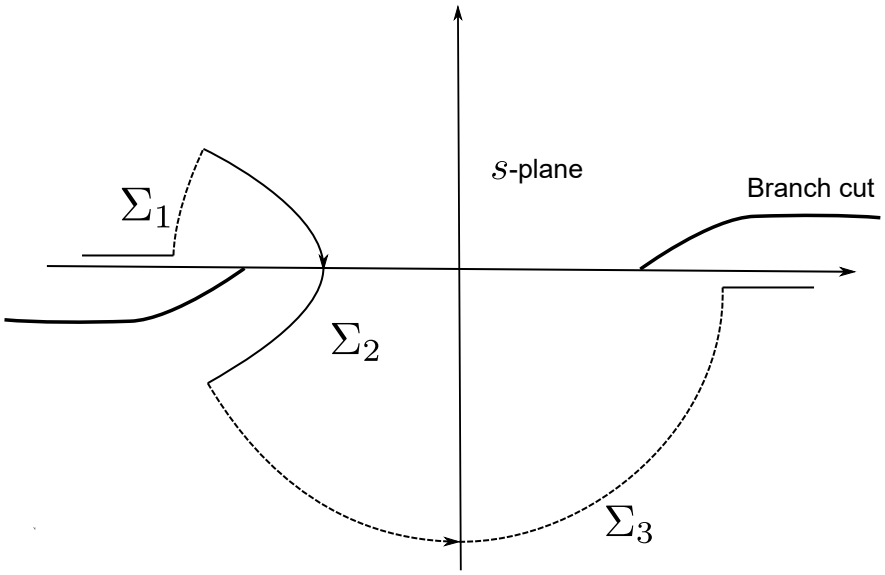

Figure 13: Deformed path when κ_n is real.

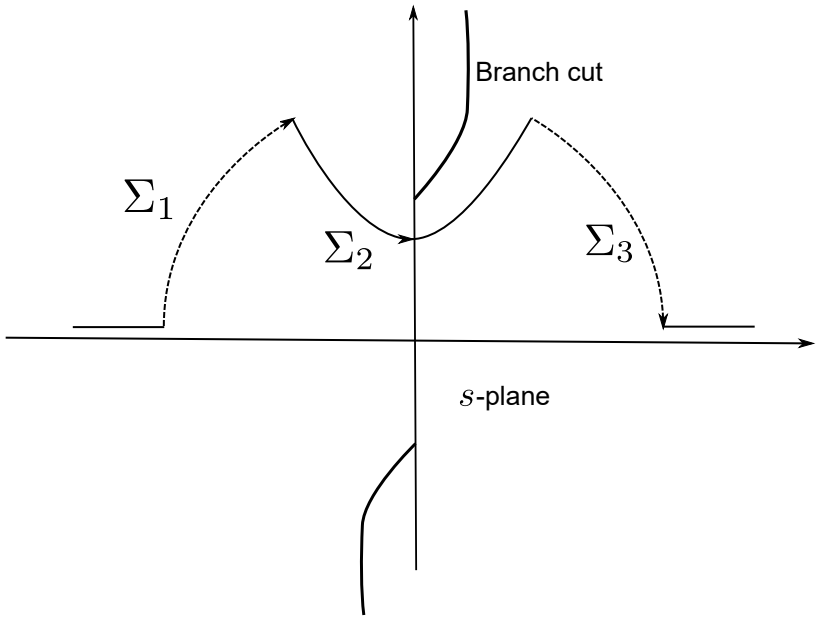

Figure 14: Deformed path when κ_n is imaginary.

where $r = \sqrt{x^2 + z^2}$.

Therefore the inversion of the Fourier transform becomes

$$\Phi(\xi, \eta, \zeta) = \frac{1}{2\pi} \sum_{n=-\infty}^{\infty} \frac{\mathrm{i} w_0 \mathrm{sgn}(\zeta) \mathrm{e}^{\mathrm{i}\chi_n \eta}}{\sqrt{-\bar{k}_1 - \kappa_n}} \int_{\Sigma_2} \frac{E_n(s)}{(s + \bar{k}_1)\sqrt{s + \kappa_n}} \mathrm{e}^{-\gamma_n |\zeta| - is(\xi + hF(\eta))} \mathrm{d}s. \tag{53}$$

Substituting equation (51) yields

$$\begin{aligned}\Phi(\xi, \eta, \zeta) =& \frac{1}{2\pi} \sum_{n=-\infty}^{\infty} \frac{\mathrm{i} w_0 \mathrm{sgn}(\zeta) \mathrm{e}^{\mathrm{i}\chi_n \eta}}{\sqrt{-\bar{k}_1 - \kappa_n}} \\ & \int_{-\infty}^{\infty} \frac{E_n(-\kappa_n \cosh(\mathrm{i}\theta + t))}{(-\kappa_n \cosh(\mathrm{i}\theta + t) + \bar{k}_1)\sqrt{-\kappa_n \cosh(\mathrm{i}\theta + t) + \kappa_n}} \mathrm{e}^{\mathrm{i}\kappa_n r \cosh t} \mathrm{d}t.\end{aligned} \tag{54}$$

In the far-field, equation (54) can be evaluated the method of stationary phase to be

$$\Phi(r, \theta, y) = \sum_{n=-\infty}^{\infty} \frac{\mathrm{e}^{\mathrm{i}\pi/4}}{\sqrt{\pi}} \frac{\mathrm{e}^{\mathrm{i}\kappa_n r}}{\sqrt{r}} \cos\frac{\theta}{2} \frac{w_0 E_n(-\kappa_n \cos\theta)}{(-\kappa_n \cos\theta + \bar{k}_1)\sqrt{-\bar{k}_1 - \kappa_n}} \mathrm{e}^{\mathrm{i}\chi_n y}. \tag{55}$$

References

[1] R. K. Amiet. Acoustic radiation from an airfoil in a turbulent stream. *Journal of Sound and Vibration*, 41(4):407–420, 1975.

[2] R. K. Amiet. High frequency thin-airfoil theory for subsonic flow. *AIAA Journal*, 14(8):1076–1082, 1976.

[3] L. J. Ayton and P. Chaitanya. Analytic solutions for reduced leading-edge noise aerofoils. In *Proceedings of 24th AIAA/CEAS Aeroacoustics Conference*, Aeroacoustics Conferences. American Institute of Aeronautics and Astronautics, 2018. AIAA 2018-3284.

[4] L. J. Ayton and P. Chaitanya. An analytical and experimental investigation of aerofoil-turbulence interaction noise for plates with spanwise-varying leading edges. *Journal of Fluid Mechanics*, 865:137–168, 2019.

[5] T. F. Brooks, D. S. Pope, and M. A. Marcolini. Airfoil self-noise and prediction. *NASA reference publication*, 1989.

[6] D. M. Bushnell and K. J. Moore. Drag reduction in nature. *Annual Review of Fluid Mechanics*, 23:65–79, 1991.

[7] P. Chaitanya and P. Joseph. Slitted leading edge profiles for the reduction of turbulence-aerofoil interaction noise. *The Journal of Acoustical Society of America*, 143:3494–3504, 2018.

[8] P. Chaitanya, S. Narayanan, P. Joseph, and J. W. Kim. Leading edge serration geometries for significantly enhanced leading edge noise reductions. In *Proceedings of 22nd AIAA/CEAS Aeroacoustics Conference*, Aeroacoustics Conferences. American Institute of Aeronautics and Astronautics, 2016. AIAA 2016-2736.

[9] P. Chaitanya, P. F. Joseph, S. Narayanan, and J. W. Kim. Aerofoil broadband noise reductions through double-wavelength leading edge serrations: a new control concept. *Journal of Fluid Mechanics*, 855:131–151, 2018.

[10] V. Clair, C. Polacsek, T. L. Garrec, G. Reboul, M. Gruber, and P. Joseph. Experimental and numerical investigation of turbulence-airfoil noise reduction using wavy edges. *AIAA Journal*, 51(11):2695–2713, 2013.

[11] D. G. Crighton, A. P. Dowling, J. E. Ffowcs Williams, M. Heckl, and F. G. Leppington. *Modern methods in analytical acoustics*. Springer-Verlag London, 1 edition, 1992.

[12] N. Curle. The influence of solid boundaries upon aerodynamic sound. *Proceedings of the Royal Society A: Mathematical, Physical and Engineering Sciences*, 231:505–514, Sep 1955.

[13] F. E. Fish, L. E. Howle, and M. M. Murray. Hydrodynamic flow control in marine mammals. *Integrative and Comparative Biology*, 48(6):788–800, 2008.

[14] J. M. R. Graham. Similarity rules for thin aerofoils in non-stationary subsonic flows. *Journal of Fluid Mechanics*, 43(04):753–766, 1970.

[15] H. Johari, C. W. Henoch, D. Custodio, and A. Levshin. Effects of leading-edge protuberances on airfoil performance. *AIAA journal*, 45:2634–2642, Nov 2007.

[16] R. Kelso K. Hansen and C. Doolan. Reduction of flow induced airfoil tonal noise using leading edge sinusoidal modifications. *Acoustics Australia*, 40 (3):172–177, 2012.

[17] J. W. Kim, S. Haeri, and P. F. Joseph. On the reduction of aerofoil-turbulence interaction noise associated with wavy leading edges. *Journal of Fluid Mechanics*, 792:526–552, 2016.

[18] A. S. H. Lau, S. Haeri, and J. W. Kim. The effect of wavy leading edges on aerofoil-gust interaction noise. *Journal of Sound and Vibration*, 332(24): 6234–6253, 2013.

[19] B. Lyu and M. Azarpeyvand. On the noise prediction for serrated leading edges. *Journal of Fluid Mechanics*, 826:205–234, 2017.

[20] B. Lyu, M. Azarpeyvand, and S. Sinayoko. A trailing-edge noise model for serrated edges. In *Proceeding of 21st AIAA/CEAS Aeroacoustics Conference*, Aeroacoustics Conferences. American Institute of Aeronautics and Astronautics, 2015. AIAA 2015-2362.

[21] B. Lyu, M. Azarpeyvand, and S. Sinayoko. Noise prediction for serrated trailing edges. *Journal of Fluid Mechanics*, 793:556–588, 2016.

[22] B. Lyu, M. Azarpeyvand, and S. Sinayoko. Noise prediction for serrated leading-edges. In *Proceeding of 22nd AIAA/CEAS Aeroacoustics Conference*, Aeroacoustics Conferences. American Institute of Aeronautics and Astronautics, 2016. AIAA 2016-2740.

[23] B. Lyu, A. Dowling, and I. Naqavi. Prediction of installed jet noise. *Journal of Fluid Mechanics*, 811:234–268, 2017.

[24] D. S. Miklosovic, M. M. Murray, and L. E. Howle. Experimental evaluation of sinusoidal leading edges. *Journal of Aircraft*, 44(4):1404–1408, 2007.

[25] M. R. Myers and E. J. Kerschen. Influence of incidence angle on sound generation by airfoil interacting with high-frequency gusts. *Journal of Fluid Mechanics*, 292:271–304, 1995.

[26] M. R. Myers and E. J. Kerschen. Influence of camber on sound generation by airfoils interacting with high-frequency gusts. *Journal of Fluid Mechanics*, 353:221–159, 1997.

[27] S. Narayanan, P. Chaitanya, S. Haeri, P. Joseph, J. W. Kim, and C. Polacsek. Airfoil noise reductions through leading edges serrations. *Physics of Fluids*, 27(025109), 2015.

[28] H. T. C. Pedro and M. H. Kobayashi. Numerical study of stall delay on humpback whale flippers. In *Proceedings of the 46th AIAA Aerospace Sciences Meeting and Exhibit*. American Institute of Aeronautics and Astonautics, 2008. AIAA 2008-584.

[29] S. Pröbsting and S. Yarusevych. Laminar separation bubble development on an airfoil emitting tonal noise. *Journal of Fluid Mechanics*, 780:167–191, 2015.

[30] C. Rao, T. Ikeda, T. Nakata, and H. Liu. Owl-inspired leading-edge serrations play a crucial role in aerodynamic force production and sound supression. *Bioinspiration and Biomimetics*, 12(046008), 2017.

[31] M. Roger and S. Moreau. Back-scattering correction and further extensions of Amiet's trailing-edge noise model. part 1: theory. *Journal of Sound and Vibration*, 286(1-2):477–506, Sep 2005.

[32] M. Roger and S. Moreau. Extensions and limitations of analytical airfoil broadband noise models. *International Journal of Aeroacoustics*, 9(3):273–305, May 2010.

[33] M. Roger, C. Schram, and L. D. Santana. Reduction of airfoil turbulence-impingement noise by means of leading-edge serrations and/ or porous materials. *19th AIAA/ CEAS Aeroacoustics Conference*, pages 1–20, 2013.

[34] M. Sanjose, A. Towne, P. Jaiswal, S. Moreau, S. Lele, and A. Mann. Modal analysis of the laminar boundary layer instability and tonal noise of an airfoil at reynolds number 150,000. *Journal of Fluid Mechanics*, 18(2-3): 317–350, 2019.

[35] L. D. Santana, J. Christophe, C. Schram, and W. Desmet. A Rapid Distortion Theory modified turbulence spectra for semi-analytical airfoil noise prediction. *Journal of Sound and Vibration*, 383(24):349–363, 2016.

[36] W. R. Sears. Some aspects of non-stationary airfoil theory and its practical application. *Journal of the Aeronautical Sciences*, 8:104–108, 1941.

[37] P. T. Soderman. Aerodynamics effects of leading-edge serrations on a two-dimensional airfoil. NASA Technical Memo X-2643, NASA, 1972.

[38] P. T. Soderman. Leading-edge serrations which reduce the noise of low-speed rotors. *NASA technical note*, 1973.

[39] J. M. Turner and J. W. Kim. Towards understanding aerofoils with dual-frequency wavy leading edges interacting with vortical distrubances. In *Proceedings of the 22nd AIAA/CEAS Aeroacoustics Conference*. American Institute of Aeronautics and Astronautics, 2016. AIAA 2016-2951.